Earth and Planetary Science Letters 290 (2010) 1–12

Contents lists available at ScienceDirect

Earth and Planetary Science Letters

journal homepage: www.elsevier.com/locate/epsl

Direct numerical simulation of two-phase flow: Effective rheology and flow patterns of particle suspensions

Y. Deubelbeiss [a,b,*], B.J.P. Kaus [b,c], J.A.D. Connolly [a]

[a] Institute for Mineralogy and Petrology, Department of Earth Sciences, ETH Zurich, 8092 Zurich, Switzerland
[b] Institute of Geophysics, Department of Earth Sciences, ETH Zurich, 8092 Zurich, Switzerland
[c] Department of Earth Sciences, University of Southern California, Los Angeles CA-90089-0740, USA

ARTICLE INFO

Article history:
Received 13 July 2009
Received in revised form 29 October 2009
Accepted 18 November 2009
Available online 13 January 2010

Editor: L. Stixrude

Keywords:
particle suspension
two-phase flow
effective properties
effective rheology
Newtonian rheology
non-Newtonian rheology
numerical simulation

ABSTRACT

We analyze the mechanical behavior of a two-phase system consisting of rigid grains and an interconnected pore fluid. For this purpose we use 2D direct numerical simulations on the spatial scale of individual grains for Newtonian and non-Newtonian fluid rheology. By using the stress–strain rate relation we derive scaling laws for effective viscosity of two-phase particle suspensions. We demonstrate that the effective rheology of the assemblage is non-Newtonian only if the fluid has a non-Newtonian rheology. At small fluid fraction, inter-granular strain rates are up to 3 orders of magnitude higher than the applied background strain rate. We suggest that this effect explains the experimentally observed change at higher strain rates in rheology, from Newtonian to non-Newtonian aggregate rheology.

To establish the conditions at which the fluid–solid aggregate deforms coherently as a consequence of Rayleigh–Taylor instabilities we studied flow patterns of particle suspensions and characterized them as a function of fluid fraction, viscosity, density, shape and size of the grains. From initial conditions with homogeneously distributed grains and interstitial fluid above a layer of pure fluid, our results show that the Rayleigh–Taylor instability dominates for moderate to large fluid fractions. At large fluid fractions, we observed a transition to a Stokes suspension mode, in which grains do not interact but sink independently. An analytical expression is derived that predicts the transition from Rayleigh–Taylor instability to Stokes suspension mode. The transition is a function of fluid fraction, radius of the grains, height of the interface and initial amplitude. Systematic numerical simulations are in good agreement with the analytical predictions.

1. Introduction

The dynamical and mechanical behaviors of particle suspensions have been examined experimentally and numerically (e.g. Ward and Whitmore, 1950; Arzi, 1978; Phan-Thien et al., 1991; Pinkerton and Stevenson, 1992; Lejeune and Richet, 1995; Costa, 2005; Caricchi et al., 2007; Costa et al., 2009). However, the effective aggregate rheology, i.e. stress and strain rate relations of particle bearing fluids is still in debate. We study the mechanical processes of two-phase particle suspensions by using direct numerical simulation on the spatial scale of individual grains, i.e. the Stokes equations are solved directly on grid points outlining each separate grain. This method facilitates the analysis and allows us to study the basic physical behavior of the dynamics of partially molten systems.

A number of studies have addressed the problem determining the viscosity of a particle suspension in Newtonian fluids as a function of particle concentration or fluid fraction, respectively. The most prominent of these is the theoretical analysis of Einstein (1906), which was modified to account for higher particle fractions by Roscoe (1952); Rutgers (1962b) reviews many similar efforts. Experimental observations (e.g., Vand, 1948; Ward and Whitmore, 1950; Arzi, 1978 or Marsh, 1981) support the theoretical models and serve as a calibration of parameters. Arzi (1978) and Rutgers (1962a) were aware of the problem of time-dependent deformation of partially molten rocks but could not quantify this effect. Recent experimental studies show a transition from Newtonian to non-Newtonian behavior with increasing higher particle fraction (e.g. Pinkerton and Stevenson, 1992; Lejeune and Richet, 1995; Caricchi et al., 2007; Champellier et al., 2008). Numerous attempts have been undertaken to expand the study of effective viscosities of particle suspensions to account for non-Newtonian rheology (e.g. Krieger and Dougherty, 1959; Gay et al., 1969; Krieger, 1972; Jeffrey and Acrivos, 1976; Costa et al., 2009; Cordonnier et al., 2009; Petford, 2009, for a review) and to derive constitutive relations between strain rate and stress for high particle fractions. Cordonnier and coworkers obtain an expression for effective viscosity of crystal-bearing melts that is a function of stress and a so-called stress dependency factor, which is a function of fluid

* Corresponding author. Institute for Mineralogy and Petrology, Department of Earth Sciences, ETH Zurich, 8092 Zurich, Switzerland. Tel.: +41 44 632 83 49; fax: +41 44 633 10 65.
E-mail address: yolanda.deubelbeiss@erdw.ethz.ch (Y. Deubelbeiss).

0012-821X/$ – see front matter © 2009 Elsevier B.V. All rights reserved.
doi:10.1016/j.epsl.2009.11.041

fraction and derived from experimental data. Costa and coworkers fit a four parameter function to experimental data for effective viscosity as a function of strain rate. The disadvantage of such models is that they use empirically derived parameters that obscure the underlying physics.

Computational studies have also contributed to the understanding of suspension mechanics, e.g., the theory of Stokesian dynamics (Brady and Bossis, 1988) accurately solves the flow of spherical suspending particles in a incompressible viscous fluid and Phan-Thien et al. (1991) use boundary element methods to solve the Stokes equations. However, computational methods have been limited to linear viscous (Newtonian) rheology and, almost invariably, spherical particles. Studies, which considered the influence of non-spherical particles showed that this does have an influence on flow patterns (e.g. Cleary, 2008), but the effective rheology of a suspension composed of spheroids or cubes was found to be similar to that of a suspension with spherical particles (Phan-Thien et al., 1991). Saar et al. (2001) used statistical models to study how the yield strength of a crystal-bearing magma depends on the particle shape, but it is difficult to estimate the effective rheology of an aggregate from this work.

In our study we employ numerical simulations with the goal of deriving scaling laws for the effective rheology of Newtonian and non-Newtonian two-phase systems. The first part of our analysis focuses on the analysis of viscosities of two-phase particle suspensions as a function of fluid fraction, strain rate, grain shape and size. The second part characterizes the flow patterns of particle suspensions. For all these analyses we use numerical models based on the finite element method (FEM). Numerical details are only very briefly outlined. The major focus of this paper is set on the description of the physical behavior of two-phase systems.

2. Model formulation: equations, numerical technique and model setup

Our mechanical model is for incompressible, Stokes flow of either Newtonian or non-Newtonian fluids. Both phases, the fluid and solid phases (melt and grains, respectively), are described by Stokes equations on the spatial scale of the individual grains. The governing equations are:

$$\frac{\partial v_i}{\partial x_i} = 0, \tag{1}$$

$$\frac{\partial \sigma_{ij}}{\partial x_j} = \rho g_i, \tag{2}$$

$$\tilde{\sigma}_{ij} = 2\mu_{\text{eff}}\,\dot{\varepsilon}_{ij}, \tag{3}$$

$$\dot{\varepsilon}_{ij} = \frac{1}{2}\left(\frac{\partial v_i}{\partial x_j} + \frac{\partial v_j}{\partial x_i}\right), \tag{4}$$

$$\sigma_{ij} = -\delta_{ij}P + \tilde{\sigma}_{ij}, \tag{5}$$

where v_i denotes velocity, $\tilde{\sigma}_{ij}$ deviatoric stress, σ_{ij} total stress, $\dot{\varepsilon}_{ij}$ strain rate, P pressure, μ_{eff} effective viscosity, ρ density, g_i gravitational acceleration, δ_{ij} the Kronecker delta and μ_{eff} is defined in Eq. (6) and Newtonian or non-Newtonian rheology is specified by choosing the power law coefficient n accordingly.

Non-Newtonian rheology is implemented by solving the system using the iteratively derived effective viscosity

$$\mu_{\text{eff}} = \mu_0(\dot{\varepsilon}_{\text{II}}/\dot{\varepsilon}_0)^{(1/n-1)}, \tag{6}$$

where $\dot{\varepsilon}_{\text{II}}$ is the second invariant of the strain rate tensor, μ_0 the characteristic viscosity and $\dot{\varepsilon}_0$ the characteristic strain rate, note that in most experimentally derived flow laws $\dot{\varepsilon}_0 = 1$. (Details to Eq. (6) are given in Appendix A.) Iteration is performed until the error for the velocity solution is sufficiently low, in this case smaller than 0.1%. For $n = 1$ the system is fully Newtonian and iterations are omitted.

The equations are solved using the finite element (FE) code MILAMIN (Dabrowski et al., 2008), which is a 2D MATLAB®-based Stokes solver. To obtain accurate solutions given the large viscosity gradients in a melt–grain system, we use a Lagrangian mesh with $P_2 - P_0$ 7-node Crouzeix–Raviart triangular elements (Cuvelier et al., 1986), which follow exactly the melt–grain boundaries. The geometry-adapted mesh is generated using TRIANGLE developed by Shewchuk (1996). This method has yield better accuracy than finite difference methods (FDM) or FEM with non-body-fitted meshes (Deubelbeiss and Kaus, 2008) for our problem configuration.

3. Effect of rheology on particle suspensions

To study the mechanical behavior as a function of material parameters and melt fraction we use a filled-box model, in which the initial spatial domain is a 2D box filled with homogeneously distributed high viscosity grains and interstitial melt (Fig. 1). The solid/melt viscosity contrast is 10^6, while this is less than the solid/melt viscosity contrast of natural systems ($>10^{15}$, McKenzie, 1984), it is adequate to describe the flow of an aggregate in which essentially all deformation is localized in the fluid. Tests of Schmid and Podladchikov (2003) (see their Fig. 2) showed that for effective viscosity contrasts $>10^3$ the grains behave as rigid particles. Additional tests to evaluate the influence of the rheology of the solid phase on the aggregate were performed and showed that the aggregate rheology is only affected by the fluid rheology, therefore a constant power law coefficient of $n = 1$ for the solid phase is assumed. Hereafter we only refer to power law coefficients of the fluid phase. We apply pure shear background strain rate boundary conditions. Model parameters (Table 1) are non-dimensionalized by using the characteristic scales given in Table 2, and all numerical calculations are done in non-dimensional form.

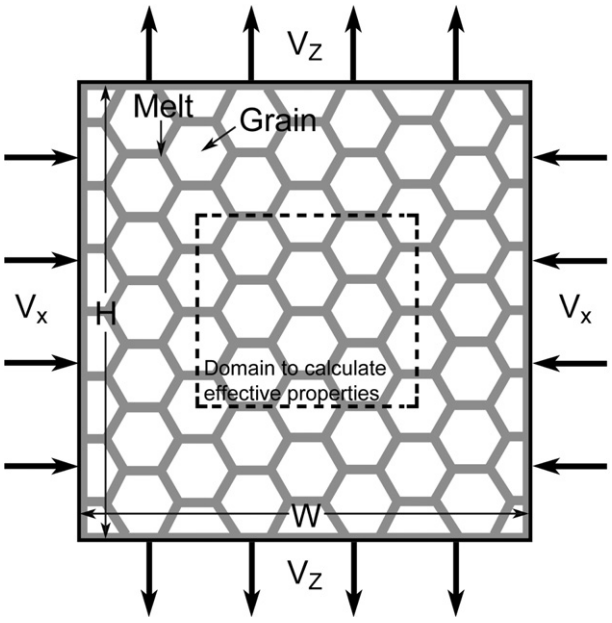

Fig. 1. Filled-box model showing pure shear boundary conditions and other parameters (Table 1). A layer of fluid is separating the grains from the boundary. Due to boundary effects effective properties are only computed in the inner box (dashed square). Depending on the test, shape and size of the grains, fluid fraction and density contrast are varied.

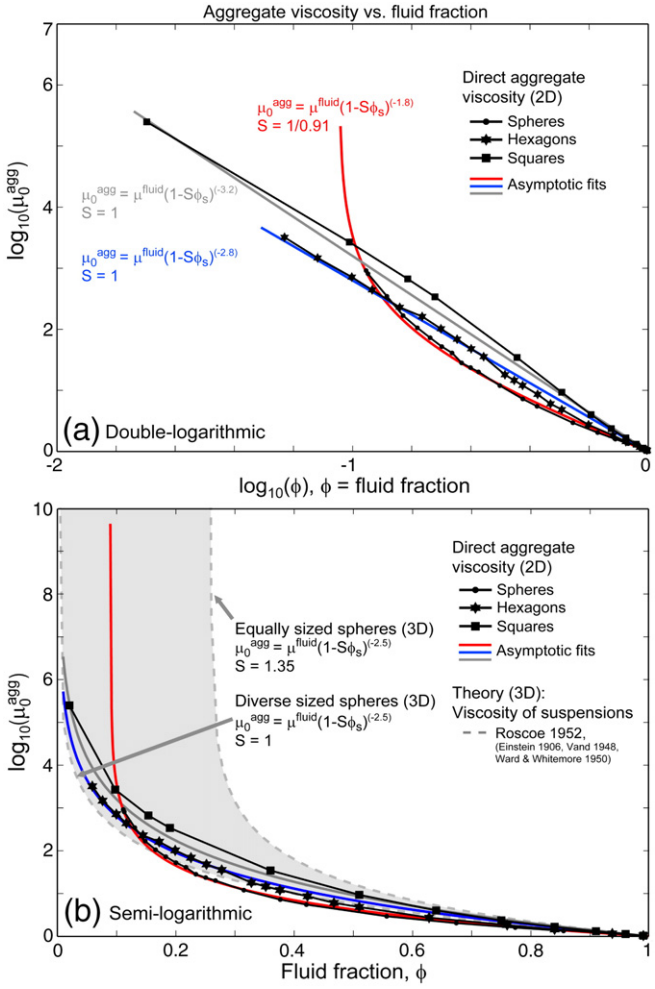

Fig. 2. Aggregate viscosity versus fluid fraction derived from numerical simulations using the stress–strain rate relationship (Eq. (7)). The aggregate viscosity is non-dimensional. (a) Double-logarithmic scale: Results are shown for three different grain shapes where for each of it an asymptotic curve is fitted. The expressions for the aggregate viscosity are for spheres $\mu_0^{agg}=\mu^{fluid}\,(1-S\phi_s)^{-1.8}$ $(S=1/0.91)$, for hexagons $\mu_0^{agg}=\mu^{fluid}\,(1-S\phi_s)^{-2.8}$ $(S=1)$ and for squares $\mu_0^{agg}=\mu^{fluid}\,(1-S\phi_s)^{-3.2}$ $(S=1)$. (b) Semi-logarithmic scale: The results from (a) and additionally the Einstein–Roscoe relationship are shown (see text for details).

3.1. Effective properties of particle suspensions

The effective properties of two-phase systems are investigated for Newtonian and non-Newtonian fluid rheology. The aggregate viscosities are derived by the macroscopic stress–strain rate relationship (Eq. (3), $n=1$), i.e. the aggregate viscosity is

$$\mu^{agg}=\frac{\tilde{\sigma}^{agg}}{2\dot{\varepsilon}^{agg}}, \tag{7}$$

Table 1
All physical filled-box model parameters are non-dimensionalized by using the characteristic scales (Table 2).

Model parameter	Value	
Width of domain	$W=1$	
Height of domain	$H=1$	
Viscosity of grains	$\mu^{grain}=10^6$	*
Viscosity of melt	After Eq. (6), for $n=1$: $\mu^{fluid}=1$	
Density of grains	$\rho^{grain}=2$	
Density of melt	$\rho^{fluid}=1$	*
Strain rate	$\dot{\varepsilon}_{BG}=1$	*

* varied for specific tests (stated in text).

Table 2
Characteristic scales of the filled-box model.

Characteristic scale	Value
Char. length scale	$L_c=H$
Char. viscosity	$\mu_c=\mu^{fluid}$
Char. time scale	$t_c=1/\dot{\varepsilon}_{BG}$

where $\tilde{\sigma}^{agg}$ and $\dot{\varepsilon}^{agg}$ are the deviatoric stresses and the strain rates averaged over the elements. Note that in the pure shear case for $\tilde{\sigma}$ and $\dot{\varepsilon}$ only pure shear components are used. The average values are calculated as follows: For each element an average value is derived by taking the mean of the values at the integration points and multiplied by the area of the element. The average of the total aggregate is then the sum of the element-wise averaged values divided by the sum of the area of each element. The effective properties are determined instantaneously before the grains move.

3.1.1. Newtonian rheology

Generally, the aggregate viscosity decreases with increasing fluid fraction (Fig. 2). Tests show that different viscosity contrasts do not influence the aggregate viscosity, provided the viscosity contrast is $>10^3$. The influence of grain size at constant fluid fraction was found to be negligible and the influence of the grain shape (spheres, hexagons, and squares) assuming high sphericity was found to be rather small, which is in agreement with previous findings (e.g. Phan-Thien et al., 1991). We use an asymptotic formulation to fit our numerically derived aggregate viscosities. This formulation is based on the Einstein–Roscoe equation (Ward and Whitmore, 1950; Roscoe, 1952), which is the modified formula of Einstein (1906) for suspensions with high particle concentrations and is given by

$$\mu_0^{agg}=\mu^{fluid}(1-S\phi_s)^{-2.5}, \text{with} \tag{8}$$

$$\phi_s=1-\phi, \tag{9}$$

$$S=\frac{1}{\phi_s^{\infty}}, \tag{10}$$

where ϕ_s is the particle fraction and ϕ the fluid fraction. S is a parameter controlling the asymptotic limit where the aggregate viscosity rises to infinity. S is the inverse of the maximum packing density ϕ_s^{∞}.

The aggregate viscosities for 2D particle suspensions as a function of fluid viscosity μ^{fluid} and fluid fraction ϕ (or particle fraction, Eq. (9)) (Fig. 2) were fitted for spheres (in 2D actually cylinders), hexagons and squares (with high sphericity) and are given by

$$\mu_0^{agg}=\mu^{fluid}(1-S\phi_s)^{m}, \tag{11}$$

with the following parameters for

Spheres	$m=-1.8$,	$S=1/0.91$
Hexagons	$m=-2.8$,	$S=1$
Squares	$m=-3.2$,	$S=1$

The original results of Roscoe compare well with our empirical relations (Fig. 2b); the discrepancies are most likely due to 2D–3D effects. In 3D, two physical end members for the range of aggregate viscosities are given by an expression on one side for a suspension of equally sized spheres and on the other side for very diverse sized spheres. In case of equally sized spheres the maximum packing density ϕ_s^{∞} is 0.74, which gives an $S=1.35$. In case of very diverse sized spheres $\phi_s^{\infty}\approx 1$, which yields an $S=1$. This represents an infinite diversification of particle sizes that can fill up the whole pore space. The factor S is therefore related to maximum packing density of the

solid particles. It is common that workers tune S in order to adequately describe a melt–grain suspension of experimental data (Roscoe, 1952; Marsh, 1981; Pinkerton and Stevenson, 1992). The reason why our 2D numerical results are shifted to the limit of very diverse spheres is most likely related to the maximum packing density ϕ_s^∞ for closest packed spheres (2D), which is in the case of 2D at $\phi_s^\infty = 0.91$. The hexagons and the squares have maximum packing densities $\phi_s^\infty = 1$ due to the highly ordered arrangement of the particles of equal size. However, the reason for the smaller exponent m of -3.2 for squares or -2.8 for hexagons instead of -2.5 (Einstein–Roscoe) is not fully clear.

3.1.2. Non-Newtonian rheology

In non-Newtonian suspensions effective aggregate viscosity is not only dependent on fluid fraction but also on strain rate. To evaluate this latter dependence we computed the effective aggregate viscosity directly for different fluid fractions, strain rates and power law coefficients and derived the following expression for the non-Newtonian effective aggregate viscosity by fitting the numerical results for spheres and hexagons:

$$\mu_{\text{eff}}^{\text{agg}} = \mu_{\text{eff}}^{\text{fluid}}(1-S\phi_s)^m(\phi^m)^{(1/n-1)}, \quad (12)$$

$$\mu_{\text{eff}}^{\text{fluid}} = \mu^{\text{fluid}}\left(\frac{\dot{\varepsilon}_{BG}}{\dot{\varepsilon}_0}\right)^{(1/n-1)}, \quad (13)$$

with the same parameters for spheres ($m=-1.8$, $S=1/0.91$) and hexagons ($m=-2.8$, $S=1$) as given for Eq. (11). $\mu_{\text{eff}}^{\text{fluid}}$ is the effective fluid viscosity and dependent on the applied background strain rate of the aggregate ($\dot{\varepsilon}_{BG}$), the characteristic strain rate $\dot{\varepsilon}_0$ and the fluid viscosity μ^{fluid}, ϕ_s is the particle fraction $(1-\phi)$ and n the power law coefficient.

The dependence of the effective aggregate viscosity on the factor $(\phi^m)^{(1/n-1)}$ can be explained analytically with a 1D model as shown in Appendix C. This factor originates from higher strain rates occurring in the fluid compared to the applied background strain rate. With decreasing fluid fraction, the strain rates in the fluid are increasing. The higher strain rates directly affect the effective viscosity in the fluid. The ratio of the effective aggregate viscosity versus the effective background viscosity depends on the fluid fraction and the power law coefficient. The relation of the exponent m of -1.8 for spheres or -2.8 for hexagons remains to be explained, but is likely related to the shape of the particles as described in Section 3.1.1.

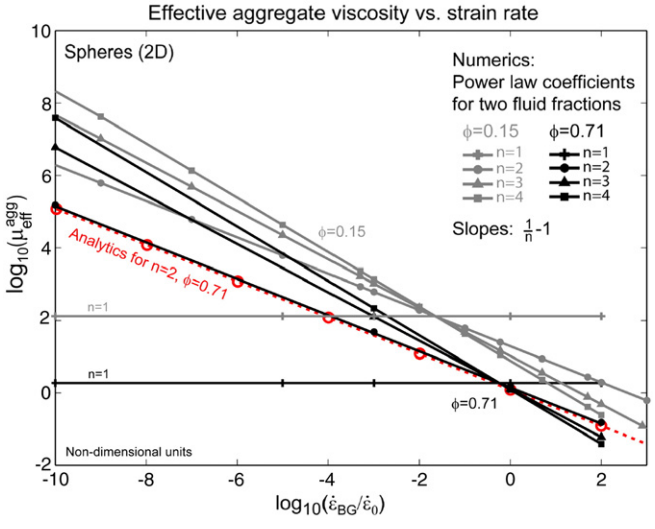

Fig. 3. Effective aggregate viscosity as a function of strain rate for different fluid fractions ($\phi=0.15$ and 0.71) and power law coefficients ($n=1$ to 4) using spherical grain shapes. Effective aggregate viscosities and strain rates are given in non-dimensional units. With increasing strain rate and fluid fraction the effective aggregate viscosity is decreasing. For $n=1$ the particle suspension has constant aggregate viscosities (Eq. (11)). The results using the analytical expression for the effective aggregate viscosity (Eq. (12)) are shown exemplified for $\phi=0.71$ and $n=2$. The analytical results are in good agreement with the numerical results.

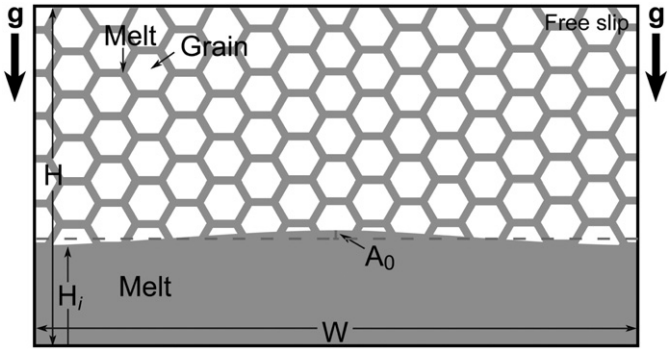

Fig. 4. Two-layer model showing free slip boundary conditions and other parameters (Table 3). Initial tests without sinusoidal perturbation but slightly perturbed individual grains always developed instabilities with parameter specific dominant wavelengths (Rayleigh–Taylor instability, discussed in Section 4.1). For systematic testing and aggregate viscosity calculations a sinusoidal perturbation with initial amplitude A_0 of one wavelength corresponding to the box size W is implemented. Depending on the test shape and size of the grains, fluid fraction, density contrast and box size were varied.

Numerical results of simulations with spherical and hexagonal grain shapes at different fluid fractions compare well with the effective aggregate viscosities predicted by Eq. (12) (Fig. 3). The effective aggregate viscosity decreases with increasing fluid fraction and increasing strain rate. The change in the effective aggregate viscosity with strain rate is $(1/n-1)$, which corresponds to the power law coefficients in Eq. (12). In contrast, for Newtonian rheology ($n=1$) of the fluid phase the aggregate viscosity remains constant throughout the computed range of strain rates, i.e. suspensions of rigid particles only behave non-linearly if the fluid phase has a non-Newtonian rheology. Effects of different grain shapes and sizes are minor.

4. Flow patterns of particle suspensions

To study flow patterns as a function of fluid fraction and fluid rheology we use a two-layer model (Fig. 4) consisting of a layer of homogeneously distributed high viscosity grains and interstitial melt overlying a layer of pure melt. The two-layer model is driven by gravity applying free slip boundary conditions at all four sides of the domain. All model parameters (Table 3) are non-dimensionalized by using the characteristic scales given in Table 4.

4.1. Rayleigh–Taylor instability mode

Initial tests of two-layer models (Fig. 4) with only slightly perturbed individual grains (perturbation: 0.1% of grain radius) rather

Table 3
All physical two-layer model parameters are non-dimensionalized by using the characteristic scales (Table 4).

Model parameter	Value	
Width of domain	$W=\lambda$	*
Height of domain	$H=1$	
Viscosity of grains	$\mu^{\text{grain}}=10^6$	*
Viscosity of melt	$\mu^{\text{fluid}}=1$ or after Eq. (6) for non-Newtonian rheology	
Density of grains	$\rho^{\text{grain}}=2$	
Density of melt	$\rho^{\text{fluid}}=1$	*
Gravity	$g=1$	
Amplitude	$A_0=0.0064$	

* varied for specific tests (stated in text).

Table 4
Characteristic scales of the two-layer model.

Characteristic scale	Value
Char. length scale	$L_c = H$
Char. viscosity	$\mu_c = \mu^{\text{fluid}}$
Char. stress	$\sigma_c = \Delta\rho g H$

than using the sinusoidal perturbation with initial amplitude as displayed in Fig. 4, show strong interactions between individual grains. The layer of grains (top layer) behaves as a homogeneous layer with aggregate viscosity (Eq. (11)) and density resulting from the two phases. The flow patterns have the characteristics of Rayleigh–Taylor (RT) instabilities resulting from a density inversion (e.g. Biot and Odé, 1965; Burg et al., 2004) or in other words, in our two-layer setup the RT instabilities are characterized by the amount of particles in the top layer, which results in an aggregate density.

Thus, with the two-layer setup we estimate the aggregate properties of the two-phase top layer by making use of the analytical solution for RT instabilities (Biot and Odé, 1965; Whitehead, 1988). The growth rate of the instability is a function of viscosity, density, gravity, wavelength and height of interface of two homogeneous layers. All physical parameters of the lower (pure melt) and top (melt–grain mixture) layer are known except the aggregate viscosity of the top layer, assuming that the aggregate density is an arithmetic average of the densities of each phase fraction. By systematically measuring the growth rate and comparing the numerical calculated growth rates with the analytical solution it is possible to fit a value for the aggregate viscosity of the two-phase top layer. In the mode where the instability can be described by the Rayleigh–Taylor limiting model, the density contrast between grains and the fluid does not affect the aggregate viscosity. These results are generally in agreement with the formerly directly calculated aggregate viscosities using the filled-box model (Eq. (11)), however aggregate viscosities derived through RT instabilities are typically larger (see Appendix B).

4.2. Transition from Rayleigh–Taylor instability to Stokes suspension mode

The homogenization and collective behavior of the grains in suspension is only valid up to a certain fluid fraction, where a clear transition is observed from the development of RT instabilities to a mode in which the grains simply sink through the fluid, the Stokes suspension mode. Such transitions have been observed experimentally by Bagdassarov et al. (1996), who describe the transition between different percolation processes analytically. However, a thorough discussion on the different governing parameters is missing. We define this transition analytically to be the condition at which the velocity of the growing RT instability (Eq. (14)) is the same as the velocity of sinking particles (Eq. (15)), the Stokes velocity. The Stokes velocity used for this analysis is based on the equation for a sinking infinite cylinder (2D) inside a finite box (Slezkin, 1955; Popov and Sobolev, 2008).

$$V_{\text{RT}} = q_{\text{dom}} A_0, \tag{14}$$

$$V_{\text{STOKES}} = f\frac{Nr^2\Delta\rho g}{4\mu^{\text{fluid}}}, \tag{15}$$

$$N = \ln(k) - \frac{k^2-1}{k^2+1}, \tag{16}$$

$$k = \frac{d}{r} \tag{17}$$

Eq. (15) is modified in a way to adapt a multi-cylinder problem, where N is here the correcting factor for the influence of the neighboring particles (Eq. (16)) rather than the wall effect described in Popov and Sobolev (2008). d is the distance between two grains (outer boundary of the grain) and r is the radius of the grain (Eq. (17)). The factor f (Eq. (15)) corrects for the offset between the analytics and the numerics. g is gravity, $\Delta\rho$ the density difference and μ^{fluid} the fluid viscosity.

The solution for the dominant growth rate q_{dom} (the wavelength for which the instability grows fastest) is a function of gravity, height of interface, density difference and viscosity contrast between the top two-phase and bottom layer. The derivation of the equations for two layers with one intersecting boundary is given e.g. by Ramberg (1968) (see also Kaus, 2005, Chp. 7). For our study we use this full perturbation analysis as well as a simplification of the full set of equations. For simplification we derive a scaling law for the dominant growth rate q_{dom} of a RT instability with free slip boundary conditions and an interface at location H_i/H, where H_i is measured from the bottom. The full form shows clearly defined regions where q_{dom} is constant within a certain parameter space for H_i/H and R. For the most relevant parameter space we derived a law, which is valid for viscosity contrasts larger than about 1000 and H_i/H larger than about 0.3 and is given in dimensionless form by

$$q_{\text{dom}} = \frac{1}{4}R^{-1}\left(1-\frac{H_i}{H}\right), \tag{18}$$

$$R = \frac{\mu_{\text{top}}}{\mu^{\text{fluid}}}, \tag{19}$$

where R is the viscosity contrast of the two-phase top layer (μ_{top}) and the underlying fluid layer (μ^{fluid}). μ_{top} is equivalent to μ_0^{agg} (Eq. (11)) of the top layer, μ_{top} is used as a simplification. Implementing Eqs. (18) and (19) in dimensional form using the characteristic growth rate $q_c = \Delta\rho g H/\mu^{\text{fluid}}$ in Eq. (14) leads to

$$V_{\text{RT}} = \frac{1}{4}\frac{A_0\left(1-\frac{H_i}{H}\right)(1-\phi)\Delta\rho g H}{\mu_{\text{top}}}. \tag{20}$$

The relative importance of the RT and Stokes suspension mode can be assessed from the parameter $Yo = V_{\text{RT}}/V_{\text{STOKES}}$. After substituting the expression for μ_{top} (Eq. (11)) in Eq. (20) and Eqs. (16) and (17) in Eq. (15) we obtain

$$Yo = \frac{A_0(H-H_i)(1-\phi)(d^2+r^2)}{f(\ln(d/r)d^2 + \ln(d/r)r^2 - d^2 + r^2)r^2(1-S(1-\phi))^m}. \tag{21}$$

The distance between two grains d can be replaced by an expression dependent on fluid fraction ϕ and radius of the grains r. This expression is given for spheres (2D) and hexagons by

$$d_{\text{spheres}} = \sqrt{\frac{r^2\pi}{2\sqrt{3}(1-\phi)}} - r, \tag{22}$$

$$d_{\text{hexagons}} = \frac{r}{\sqrt{1-\phi}} - r. \tag{23}$$

For hexagons using for d Eq. (23) and for μ_{top} Eq. (11) ($m = -2.8$ and $S = 1$) Yo results in

$$Yo = \frac{A_0\phi^{2.8}(H-H_i)(1-\phi)((r/\sqrt{1-\phi}-r)^2+r^2)}{f(\ln((r/\sqrt{1-\phi}-r)/r)(r/\sqrt{1-\phi}-r)^2 + \ln((r/\sqrt{1-\phi}-r)/r)r^2-(r/\sqrt{1-\phi}-r)^2+r^2)r^2}. \tag{24}$$

Yo is thus a function of fluid fraction ϕ, radius of the grains r, height of the interface H and initial amplitude A_0. A transition from RT

to Stokes suspension mode is expected at $Yo=1$ when the RT velocity and the Stokes velocity are equal.

To assess the accuracy of our analytical expression we perform numerical simulations. To classify the numerical results we use the numerical transition number (NTR), defined as

$$NTR = \frac{|V_{\text{center}}| + |V_{\text{bound}}|}{sign(V_{\text{center}})}, \quad (25)$$

where V_{center} is the velocity in the center of the boundary between the lower and upper layers and V_{bound} is the velocity at the boundary of the box between the lower and upper layers (Fig. 5). If NTR is positive then the center velocity has a positive value, meaning that and upward RT instability is occurring, while negative NTRs imply that grains are sinking everywhere and indicate a Stokes suspension mode.

The transition from RT instability to Stokes suspension mode ($Yo=1$) predicted by our simplified expression (Eq. (24)) and by the complete perturbation analysis for hexagonal grains is depicted in Fig. 6. The numerical results for simulations performed for different grain sizes and distances between grains are plotted with the analytically derived transition (Fig. 6a). The analytical transition ($Yo=1$) using the perturbation analysis is in agreement with the numerical results. The dependence of $Yo=1$ on fluid fraction ϕ and radius r (Fig. 6b) shows that even for variations of A_0/H or H_i/H, large fluid fractions are required to achieve the Stokes suspension mode.

4.3. Flow patterns for randomly perturbed systems

The influence of fluid rheology on the flow pattern was studied starting with randomly perturbed grains and a box several times the size of the developing dominant wavelength. Here, we assume a two-layer model that has in both layers two phases. The upper layer has a fluid fraction of $\phi_{\text{top}}=0.31$ and the lower one has smaller grains and a fluid fraction of $\phi_{\text{bottom}}=0.48$. The simulation with Newtonian rheology (Fig. 7, top) shows development of RT instabilities with a wavelength $\lambda \approx 2/H$. This value is also predicted by the analytical solution for the dominant wavelength for the corresponding aggregate viscosities. The simulation with non-Newtonian rheology ($n=2$ for the fluid phase) (Fig. 7, bottom) still develops the large scale RT instabilities of the same wavelength. One can argue whether there are smaller scaled channels formed that localizes the deformation, however to prove this more systematic simulations are required.

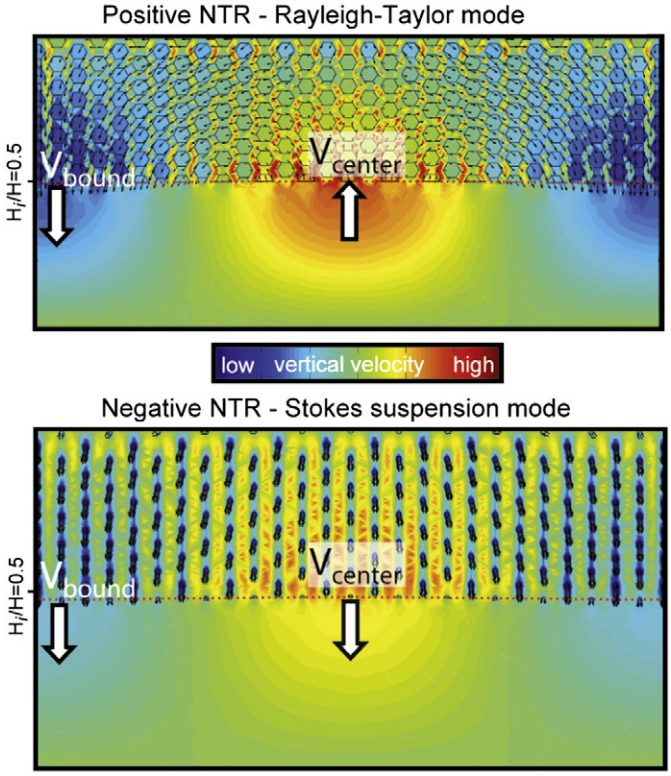

Fig. 5. Numerical simulations of two-phase two-layer model with an interface at $H_i/H=0.5$. For $\phi=0.61$, where $r=0.029$ and $d=0.03$ the NTR is positive representing a RT instability, while for $\phi=0.97$, where $r=0.076$ and $d=0.07$ the NTR is negative and all grains directly sink down. The color scale indicates the vertical velocity.

5. Discussion on rheology: comparison with experiments

The numerical results of the effective aggregate viscosity of particle suspensions for different rheologies as described in the previous sections reveal an abrupt reduction in the effective aggregate viscosity at melt fractions between 10 and 30% irrespective of the rheology. This is a common experimental observation (e.g. Vand, 1948; Ward and Whitmore, 1950; Arzi, 1978; Lejeune and Richet, 1995; Caricchi et al., 2007). Additionally, it is commonly observed that aggregate rheology becomes non-Newtonian at high particle fractions (e.g. Krieger, 1972; Jeffrey and Acrivos, 1976; Pinkerton and Stevenson, 1992; Stickel and Powell, 2005; Costa, 2005; Caricchi et al., 2007; Cordonnier et al., 2009, for a review). Experiments of Caricchi et al. (2007) show that the effective aggregate viscosity is not only dependent on fluid fraction but also on strain rate. This non-Newtonian behavior was observed between about $\dot{\varepsilon}_{\text{shear}}=10^{-5}\,\text{s}^{-1}$ and $\dot{\varepsilon}_{\text{shear}}=10^{-3}\,\text{s}^{-1}$. While Caricchi and coworkers's results show non-Newtonian behavior (i.e. strain–rate dependent effective viscosity) only above a certain strain rate, our numerical results using non-Newtonian rheology described by Eq. (12) showed this effect over the whole range of strain rates. On the other hand, simulations using a power law coefficient of $n=1$ showed independent of the strain rate the same effective aggregate viscosity. This implies that our modelled system only behaves non-linearly if the melt has a non-Newtonian rheology (Fig. 3). This is in contrast to the statement of Caricchi and coworkers who suggest that the non-Newtonian behavior they observe in their experiments is induced by a rearrangement of grains, while the melt itself behaves Newtonian. Their assumption that melt is Newtonian is based on experiments of pure melt performed by Webb and Dingwell (1990) giving a range of temperature and strain rates where the fluid (melt) phase does not exceed the “relaxed” Newtonian mode. A non-Newtonian behavior of the melt, however, was observed for higher strain rates (e.g. $>5\times10^{-5}\,\text{s}^{-1}$ for a shear viscosity of 10^{12} Pa s). It is thus important to understand what the strain rate of the melt is inside a deforming two-phase aggregate.

5.1. Can locally enhanced strain rates explain non-Newtonian behavior?

Numerical models using either Newtonian or non-Newtonian rheology show that the applied background strain rate of the system is not the local strain rate distribution inside the system (Fig. 8). Channels form between the grains, where the strain rates of the second invariant are significantly larger than the applied background strain rate. The excess of strain rate is $\dot{\varepsilon}_{\text{II,max}}/\dot{\varepsilon}_{\text{BG}}=48$ for a fluid fraction of 0.23 with spherical shaped grains. In order to understand the dependency of $\dot{\varepsilon}_{\text{II,max}}$ on fluid fraction, we performed systematic numerical simulations that were fitted with an asymptotic formulation (Fig. 9). Results show that $\dot{\varepsilon}_{\text{II,max}}$ is a function of the background strain rate $\dot{\varepsilon}_{\text{BG}}$, fluid fraction ϕ and geometry factor S known from the Einstein–Roscoe equation (Eq. (8)) and are given for 2D spherical shaped grains and for hexagons by

$$\dot{\varepsilon}_{\text{II,max}} = 2\dot{\varepsilon}_{\text{BG}}(1-S\phi_s)^m, \quad (26)$$

with $m=-1.6$ and $S=1/0.91$ for spheres and $m=-2.4$ and $S=1$ for hexagons. The formula obeys two limits: One limit is the minimum

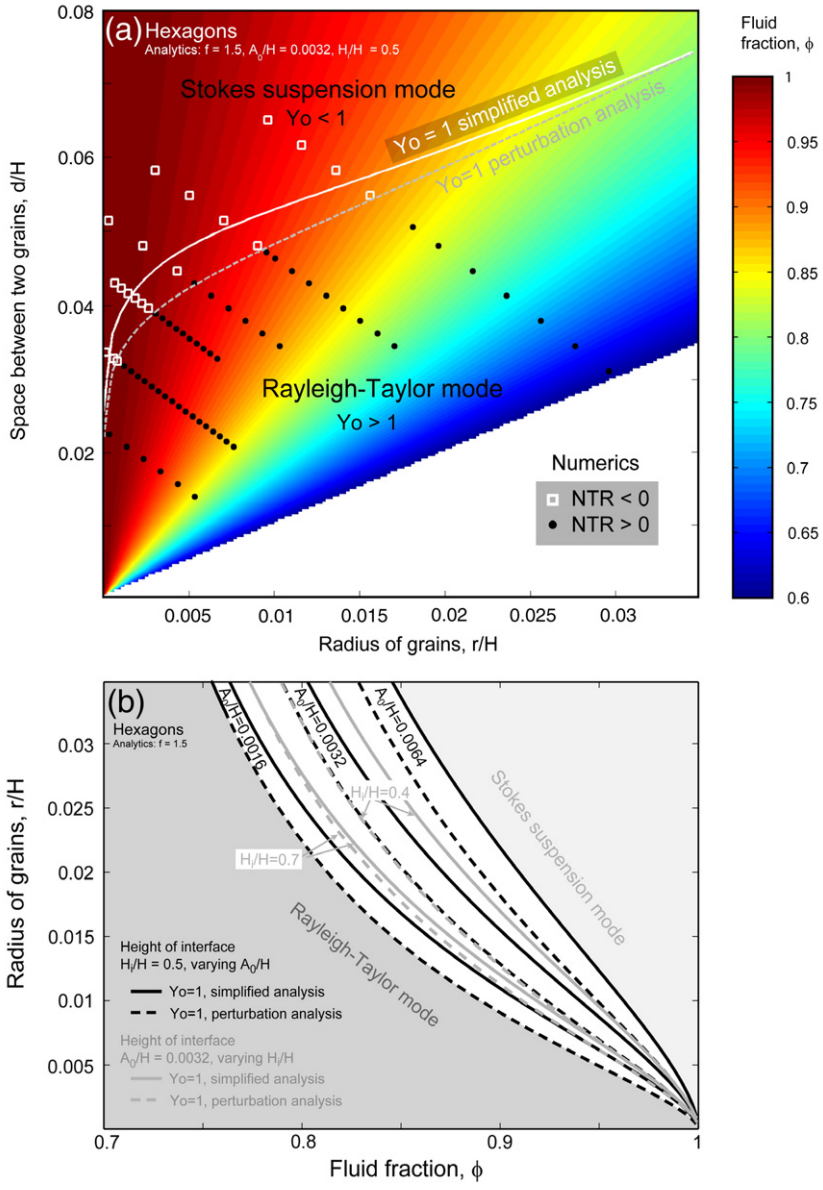

Fig. 6. Transition from RT mode to the Stokes suspension mode for hexagonal shaped grains (a) as a function of fluid fraction ϕ, normalized radius of the grains r and the normalized distance between two grains d for an interface at $H_i/H=0.5$ and initial amplitude $A_0/H=0.0032$. The color map represents the ϕ-distribution as a function of r and d (for hexagons $\phi=1-r^2/(r+d)^2$). $Yo=1$ is shown for the simplified analysis as derived in the text and for the full form of the perturbation analysis. Black dots are numerical simulations with positive numerical transition numbers (NTR) and the white squares are numerical simulations with negative NTRs, (b) as a function of fluid fraction ϕ, normalized radius of the grains r for different initial amplitudes A_0/H and height of interfaces H_i/H.

value of $\dot{\varepsilon}_{II,max}/\dot{\varepsilon}_{BG}=2$. This limit is based on the analytical solution of the perturbation flow field around a rigid circular grain, which reaches a finite maximum strain rate that is twice the applied far-field strain rate, for both simple and pure shear, independent of inclusion size (Schmid and Podladchikov, 2003). The second is an asymptotic limit and is given by the maximum packing density σ_s^{∞}, which is for 2D spheres 0.91, i.e. for a fluid fraction of $\phi=0.09$ $\dot{\varepsilon}_{II,max}/\dot{\varepsilon}_{BG}$ increases to infinity. The same occurs for hexagons at a fluid fraction of 0, therefore the increase to infinity is not visible in Fig. 9.

For $\phi\approx 0.12$ the maximum strain rate $\dot{\varepsilon}_{II,max}$ is 2.5 orders of magnitudes higher than the applied background strain rate and reaches more than 4 orders of magnitude for $\phi\approx 0.03$. The influence of the different grain shapes and the influence of the power law coefficient (Fig. 9) are small compared to the effect of increasing strain rate with decreasing fluid fraction. The increase in strain rate is occurring in the same manner for Newtonian rheology as for non-Newtonian rheology. The increase of the maximum strain rate is related to a decrease in effective viscosity inside the fluid. This effect can be explained analytically with a 1D model (Appendix C).

Such local strain rate focusing might be one of the reasons to overcome the threshold, where pure melt rheology changes from the Newtonian viscous to the non-Newtonian viscous regime. We show that strain rates are locally larger and hence the fluid rheology may be non-Newtonian, even though the background strain rate would indicate that results are still in the Newtonian regime. While Caricchi and coworkers assume their experiments were in the "relaxed" Newtonian regime, they might locally already be above the threshold given by Webb and Dingwell (1990) where melt behaves non-linearly.

Changes in microstructures (rearrangement of the grains) under shear inside the system (Völtz et al., 2002; Stickel and Powell, 2005; Caricchi et al., 2007) are sometimes cited as a reason for strain rate dependent viscosities. Similarly, Arbaret et al. (2007) observe non-Newtonian behavior as a result of shape preferred orientations (SPO)

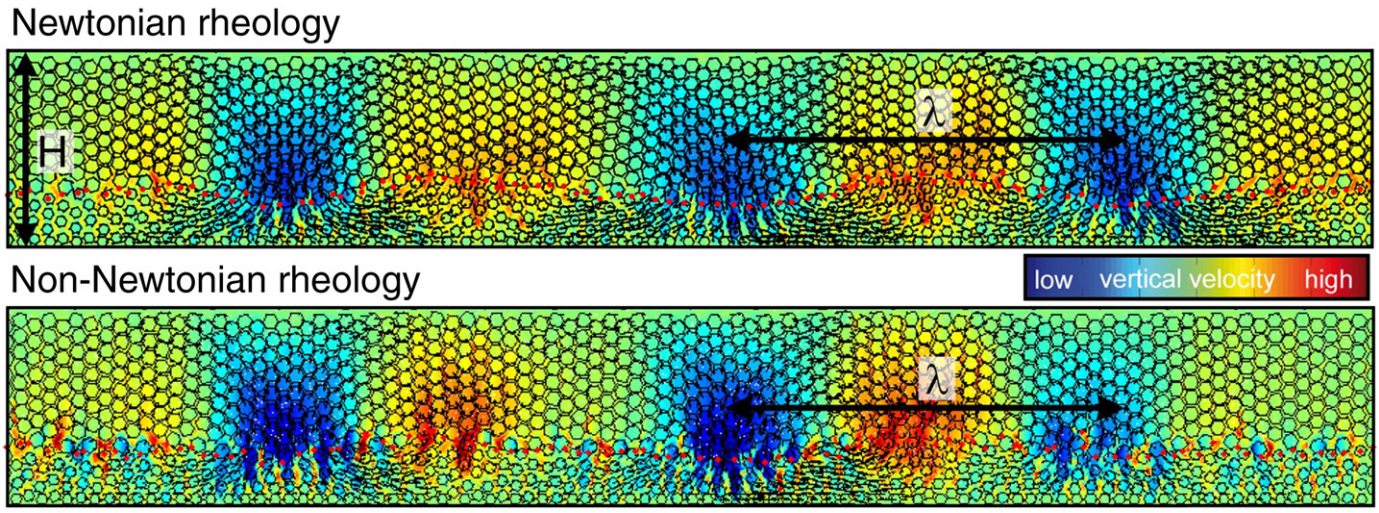

Fig. 7. Typical flow patterns for different rheologies using a two-layer model. Both layers have two phases, where $\phi_{top} = 0.31$ and $\phi_{bottom} = 0.48$. The Newtonian and the non-Newtonian simulation show Rayleigh–Taylor (RT) instabilities of a wavelength $\lambda \approx 2/H$, which is predicted by the analytical solution.

of non-spherical particles. These microstructures might cause a decrease of the aggregate viscosity for higher strains. The two-phase system has an effectively smaller anisotropic viscosity due to microstructural effects rather than a strain rate dependent viscosity. Finite strain analysis shows that for weak particles SPO develop and this results in an overall mechanical anisotropy, that lowers the aggregate viscosity (Dabrowski, 2008; Dabrowski et al., 2009). While for hard particles the reordering effect may increase the effect of locally enhanced strain rates, where channels locally become even smaller. Strain localization within the melt, which is even stronger for smaller fluid fractions might result in high strain rates that are locally built up, hence the melt has a significant amount of contact with the melt channel walls. Our suggestion is that this modifies the effective aggregate rheology of the melt.

Hess et al. (2008) hypothesize that shear heating induces the non-linear behavior of the melt viscosity, however, their experiments were performed for homogeneous samples in which the shear strain rate is likely to be homogeneous. But, as just demonstrated, shear strain rates are heterogeneous in two-phase media, which is thus likely to affect the effective rheology of the aggregate. However, to confirm this hypothesis experiments, which consider the effects of elasticity, shear heating and finite strain are required.

5.2. Complex versus simplified models

The analysis presented here uses a simplified model to describe mechanical processes in two-phase particle suspensions. The dynamical and mechanical processes may be much more complex in nature due to spatial heterogeneities of material properties in partially molten systems. Additionally, different processes may compete and overlap due to coupling of different processes such as transport of melt, melting, deformation of fluid and solid material or thermal effects due to shear heating. Costa (2005) argues that it is impossible to develop a simple description of the rheology of particle suspensions because such systems are subjected to different forces such as thermal, electrical and hydrodynamic interactions and moreover particle shapes and particle size distributions play an important role. For this reason, Costa (2005) advocates the use of empirical functions. The draw-back of such a strategy is that empirical parameters have no physical meaning.

In our models the effective aggregate viscosities are calculated after the first time step before the grains start to move. Therefore effects due to a rearrangement of the particles under shear are not directly taken into account in our model. Such an effect as well as the relative importance of elasticity, shear heating and finite strain in

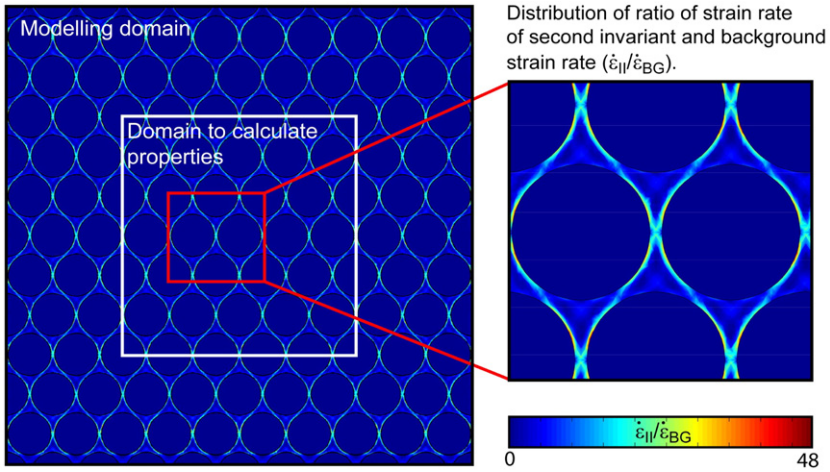

Fig. 8. Distribution of the ratio of strain rate of second invariant and background strain rate ($\dot{\varepsilon}_{II}/\dot{\varepsilon}_{BG}$) inside the melt–grain system for a fluid fraction of $\phi = 0.23$. Between two grains there are channels where the actual strain rate is much higher than the applied background strain rate. Here the excess of strain rate is $\dot{\varepsilon}_{II,max}/\dot{\varepsilon}_{BG} = 48$.

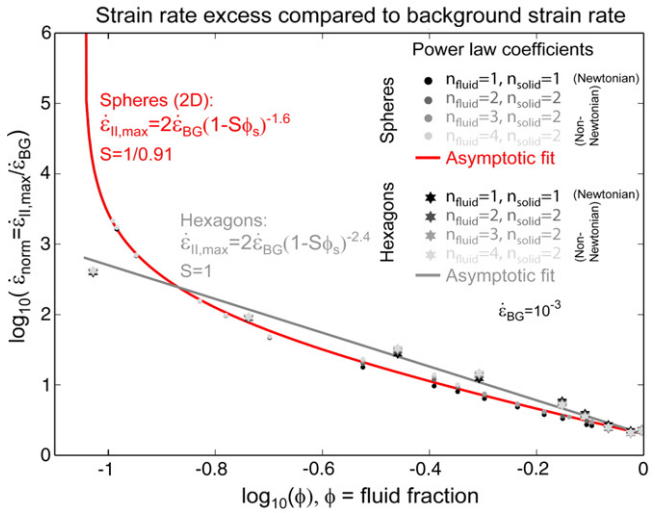

Fig. 9. The maximum strain rate of the second invariant $\dot{\varepsilon}_{II}$ normalized by the background strain rate $\dot{\varepsilon}_{BG}$ as a function of fluid fraction ϕ. The power law coefficient has hardly any effect on the general trend of increasing $\dot{\varepsilon}_{II,max}$ with decreasing ϕ. $\dot{\varepsilon}_{II,max}$ for spheres (2D) is described by $\dot{\varepsilon}_{II,max}=2\dot{\varepsilon}_{BG}\ (1-S\phi_s)^{-1.6}$, with $S=1/0.91$ and for hexagons by $\dot{\varepsilon}_{II,max}=2\dot{\varepsilon}_{BG}\ (1-S\phi_s)^{-2.4}$ with $S=1$. There are two limits: A minimum value for $\dot{\varepsilon}_{II,max}/\dot{\varepsilon}_{BG}=2$ and maximum fluid fraction ϕ depending on the maximum packing density ϕ_s^m at which $\dot{\varepsilon}_{II,max}/\dot{\varepsilon}_{BG}$ rises to infinity (see text for details).

particle suspensions under shear should be examined in future using finite strain experiments that compare the results of numerical simulations directly to experimentally derived data.

The derived scaling laws from simple model setups can be applied e.g. to predict the mechanical mode in which two-phase petrological experiments should be performed, so that the setup can be chosen for the parameter of interest. Rayleigh–Taylor instabilities, for example, might have a strong influence on the time scale of percolation and settling velocities of particles in partially molten systems. Similarly, Golabek et al. (in press) see in core formation experiments strong interactions of heavy iron droplets inside a silicate melt, the wavelength of up- and downwellings of collected iron droplets could be predicted assuming that the perturbations are related to Rayleigh–Taylor instabilities.

6. Conclusions

We studied the effect of fluid rheology on two-phase particle suspensions using direct numerical simulation and we derived expressions to calculate effective aggregate viscosities for Newtonian and non-Newtonian rheology. Our results show that the rheology of the fluid phase governs the effective aggregate rheology of the two-phase assemblage, i.e. particle suspensions only behave non-Newtonian if the fluid phase has non-linear rheology, irrespective of the rheology of the solid phase. Locally enhanced strain rates inside particle suspension might cause the change from Newtonian to non-Newtonian rheology at higher particle fractions.

We parameterized typical flow patterns and derived an analytical solution for the change from Rayleigh–Taylor instability (strongly interacting particles, homogenization of two-phase layer) to Stokes suspension (independently sinking particles) mode. The transition generally occurs at high fluid fractions (>0.8). Randomly perturbed two-layer two-phase models of Newtonian as well as non-Newtonian rheology develop Rayleigh–Taylor instabilities with dominant wavelength according to the aggregate viscosity and density.

Further investigation for direct comparison between experimental and numerical studies of partially molten systems is required. Finite strain experiments with more sophisticated models would give insights into the relative importance of shear heating, non-Newtonian melt rheologies, elasticity on the effective rheology of the assemblage.

Acknowledgements

This work was supported by the Swiss National Science Foundation grant 200021-107889. Helpful discussion with Marcin Dabrowski about numerical issues concerning the code MILAMIN and effective properties of two-phase media are gratefully acknowledged. We further thank the reviewers namely Benoit Cordonnier and Harro Schmeling for insightful and helpful reviews, which helped to improve the manuscript significantly.

Appendix A. Equation for non-Newtonian rheology — effective viscosity

The equation for the strength in case of power law creep in the lithosphere is generally described by (Ranalli, 1995, 1997):

$$\sigma = \left(\frac{\dot{\varepsilon}}{A}\right)^{1/n} \exp\left(\frac{E}{nRT}\right) \tag{27}$$

where σ is the principal stress difference, $\dot{\varepsilon}$ the strain rate, T the absolute temperature, R the universal gas constant, n the power law coefficient and A and E are creep parameters of the material. Our numerical simulations are isothermal experiments, therefore we reduce the equation to the general form (Ranalli, 1995, Chp. 4.4)

$$\tilde{\sigma}_{ij} = C\dot{\varepsilon}_{II}^{(1/n-1)}\dot{\varepsilon}_{ij}, \tag{28}$$

where $\tilde{\sigma}_{ij}$ is the deviatoric stress tensor, $\dot{\varepsilon}_{II}$ the second invariant of the strain rate tensor, $\dot{\varepsilon}_{ij}$ the strain rate tensor and C is, in general, a function of pressure, temperature and material parameters and is according to Eq. (27)

$$C = \left(\frac{1}{A}\right)^{(1/n-1)} \exp\left(\frac{E}{nRT}\right). \tag{29}$$

Eq. (28) is expanded by a characteristic strain rate $\dot{\varepsilon}_0$ which results in

$$\tilde{\sigma}_{ij} = C\left(\frac{\dot{\varepsilon}_{II}}{\dot{\varepsilon}_0}\right)^{(1/n-1)} \dot{\varepsilon}_0^{(1/n-1)} \dot{\varepsilon}_{ij}. \tag{30}$$

The deviatoric stress ($\tilde{\sigma}_{ij}$) for a viscous material is given by (Eq. (3))

$$\tilde{\sigma}_{ij} = 2\mu_{eff}\dot{\varepsilon}_{ij}. \tag{31}$$

Combining Eqs. (30) and (31) results for the effective viscosity in

$$\mu_{eff} = C\left(\frac{1}{2}\right)\left(\frac{\dot{\varepsilon}_{II}}{\dot{\varepsilon}_0}\right)^{(1/n-1)} \dot{\varepsilon}_0^{(1/n-1)}. \tag{32}$$

The power law effective viscosity is given by the following general form

$$\mu_{eff} = M\left(\frac{\dot{\varepsilon}_{II}}{\dot{\varepsilon}_0}\right)^{(1/n-1)}, \tag{33}$$

where in case of Newtonian rheology, $n=1$, we get $M=\mu_0$, the characteristic viscosity of the material. M is a material parameter and has for $n>1$ the units $\mathrm{Pa}\times\mathrm{s}^{1/n}$. Since M has only a known value for $n=1$, we use for $n>1$ the characteristic viscosity μ_0 and a

characteristic strain rate $\dot{\varepsilon}_0$, which leads to the following form (used for numerical implementation Eq. (6)) with correct dimensions

$$\mu_{\text{eff}} = \mu_0 \left(\frac{\dot{\varepsilon}_{\text{II}}}{\dot{\varepsilon}_0} \right)^{(1/n-1)}. \tag{34}$$

From Eqs. (32) and (34) follows that

$$\mu_0 = C \left(\frac{1}{2} \right) \dot{\varepsilon}_0^{(1/n-1)}, \tag{35}$$

which shows the relationship of the characteristic viscosity μ_0, the characteristic strain rate $\dot{\varepsilon}_0$ and the material parameter C.

Appendix B. Viscosity derivation in different flow fields

B.1. Viscosity derivation using Rayleigh–Taylor instabilities

The analytical solution for RT instabilities (Biot and Odé, 1965; Whitehead, 1988) is used to derive the aggregate viscosity of the top layer of the two-layer model (Fig. 4). The growth rate of the instability is a function of viscosity, density, gravity, wavelength and height of interface of two homogeneous layers. To compare the growth rate curves of the analytical solution with the numerical solution the growth rate for the two-layer model was calculated for different box sizes, i.e. for different wavelengths but with constant parameters for the two phases (fluid and grains) as well as constant fluid fraction. Fig. 10a shows the growth rate curves as a function of wavelengths normalized by the height of the box H for different fluid fractions. Due to the fact that all physical parameters of the lower (pure fluid) and top (fluid–grain mixture) layer are known except the aggregate viscosity of the top layer, assuming that the aggregate density is an arithmetic average of the densities of each phase fraction, the aggregate viscosity of the top layer can then be found by manually fitting the analytical solution.

The aggregate viscosities are evaluated using the RT instability fitting method for different grain shapes (Fig. 10b). The viscosities derived by the RT instability fitting method are typically higher than the directly derived viscosities using the stress–strain rate relationship (Eq. (7)). The values are not systematically higher, e.g. for squares both methods are in agreement while for spheres the misfit is almost a factor 2. The higher values for the RT instability fitted viscosities are not fully understood. This discrepancy might be due to the fact that RT instabilities produce a more general strain rate field composed of pure and simple shear components, rather than a purely pure shear flow field in the pure shear case. Additionally, inaccuracies in measuring the growing velocity at the interface may have an influence on the results as well. Testing different velocity evaluation schemes, however, showed that this did not affect the results.

B.2. Anisotropy effects for square shaped particles

We performed additional simulations in order to test a possible effect of anisotropy of different particle shapes. In these simulations, we applied either pure shear (as in the simulations discussed in Section 3.1.1) or simple shear boundary conditions to a horizontally pronounced setup (squares horizontally shifted against each other) using square shaped grains and calculated the directly derived aggregate viscosities (Eq. (11)). For the simple shear case a significant decrease of the aggregate viscosity of approximately factor two can be observed. Simulations with either horizontally or vertically (squares vertically shifted against each other) pronounced setups were performed to calculate the aggregate viscosities using the RT fitting method (Appendix B.1). In this case the difference between the two setups is negligibly small. Applying simple shear or pure shear deformation to hexagonal or spherical shaped grains does not have a noticeable influence on the aggregate viscosities.

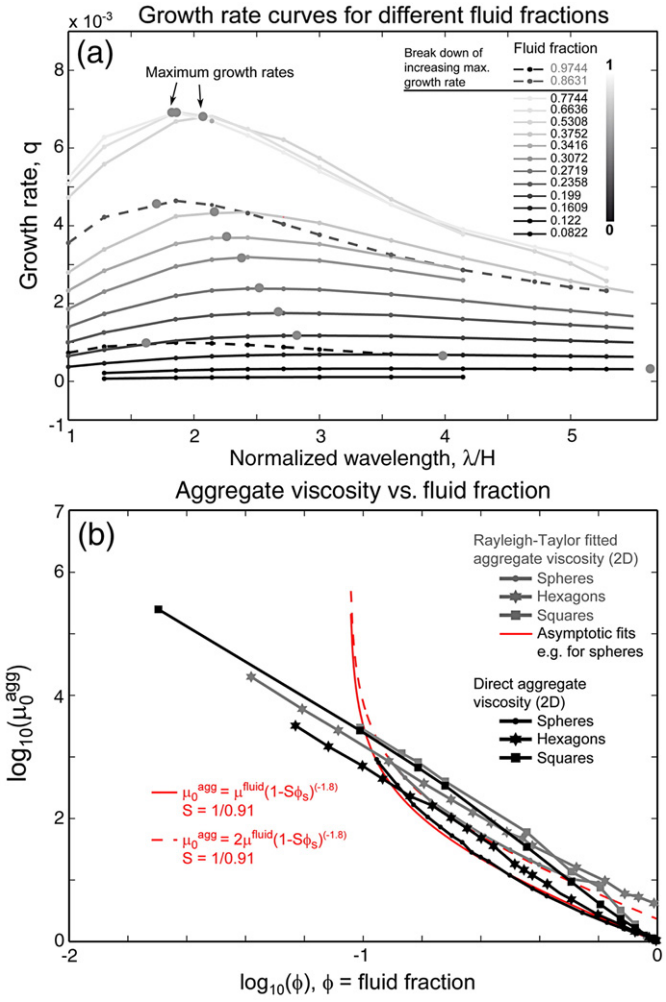

Fig. 10. (a) Growth rate curves for different fluid fractions. Each curve represents calculations with fixed parameters (fluid fraction, viscosity, density and height of interface) but changing wavelengths by changing the size of the width W (Fig. 4). (b) Aggregate viscosity versus fluid fraction in double-logarithmic scales derived using (1) the analytical solution of Rayleigh–Taylor instabilities and (2) the stress–strain rate relationship (Eq. (7)) as described in Section 3.

This generally indicates that shapes that have a low sphericity tend to influence the aggregate viscosity by an effective mechanical anisotropy in the two-phase particle suspension. In a more general flow field (combination of pure and simple shear) as it is produced in a RT instability field this effect is likely to disappear.

Appendix C. 1D model: dependence of the effective aggregate viscosity on fluid fraction in case of non-Newtonian rheology

We obtained insight in the governing parameters of a two-phase particle suspension using non-Newtonian rheology (Section 3.1.2). Due to complexity of the resulting equation (Eq. (12)) we study a 1D model to gain more information, specifically, the dependence of the effective viscosity on the fluid fraction ϕ. We consider a thin bar of length L that is composed of a fraction of fluid and grain with different constant viscosities (μ_f and μ_s) separated by an interface. The system is subjected to constant strain rate ($\dot{\varepsilon}_{\text{BG}}$) boundary conditions.

The general derivation of the 1D set of equation is given in details in Deubelbeiss and Kaus (2008). For the given setup we can assume that the stress inside the system is constant.

$$\sigma_{xx} = 4\mu \frac{\partial v_x}{\partial x}, \tag{36}$$

σ_{xx} is the stress in x direction, v_x the velocity in x direction and μ the viscosity inside the system. According to the derived Eq. (18) in Deubelbeiss and Kaus (2008) we can rewrite Eq. (36) as

$$\sigma_{xx} = \frac{4\mu_f\mu_s}{(\mu_f(1-\phi) + \mu_s\phi)}\dot{\varepsilon}_{BG}, \tag{37}$$

$$\dot{\varepsilon}_{BG} = \frac{\Delta v_x}{L}, \tag{38}$$

where $\dot{\varepsilon}_{BG}$ is the applied background strain rate, Δv_x is the velocity difference at the left and right boundary, L the length of the domain, μ_f and μ_s are the fluid and the grain (solid) viscosity, respectively. For the special case where the interface is in the center at $x=a=0$ ($\phi=0.5$) then Eq. (37) becomes

$$\sigma_{xx} = \frac{8\mu_f\mu_s}{(\mu_f + \mu_s)}\dot{\varepsilon}_{BG}. \tag{39}$$

Assuming a non-Newtonian rheology for the fluid (grain rheology remains Newtonian) we substitute in Eq. (37) μ^f_{eff} by

$$\mu^f_{eff} = \mu_0\left(\frac{\dot{\varepsilon}^f_{xx}}{\dot{\varepsilon}_0}\right)^{(1/n-1)} \tag{40}$$

where μ_0 is a characteristic viscosity (see Section 2, Appendix A) and $\dot{\varepsilon}^f_{xx}$ the strain rate inside the fluid. The strain rate of the fluid $\dot{\varepsilon}_{xx}$ is according to Eq. (36) and substituting Eqs. (37) and (40)

$$\dot{\varepsilon}^f_{xx} = \frac{\mu_s}{\mu_0\left(\frac{\dot{\varepsilon}^f_{xx}}{\dot{\varepsilon}_0}\right)^{(1/n-1)}(1-\phi) + \mu_s\phi}\dot{\varepsilon}_{BG}. \tag{41}$$

The equation is rather difficult to solve for an arbitrary n. For $n>4$ the solution can only be derived numerically. Therefore we exemplarily show the solution for the case $n=2$. In this case there are 3 possible solutions, where only one is realistic for our case

$$\dot{\varepsilon}^f_{xx} = \frac{1}{2\mu_s^2}\left(4\mu_s^2\dot{\varepsilon}_{BG} + \mu_0^2 + \mu_0^2\sqrt{\frac{8\mu_2^2\dot{\varepsilon}_{BG} + \mu_0^2}{\mu_0^2}}\right). \tag{42}$$

By knowing $\dot{\varepsilon}^f_{xx}$ we can calculate the effective fluid viscosity μ^f_{eff} (Eq. (40)). Thus, the effective aggregate viscosity of the whole system μ^{agg}_{eff} (derivation of μ^{agg}_{eff} see Deubelbeiss and Kaus (2008)) as well as the background aggregate viscosity μ^{agg}_{BG} is

$$\mu^{agg}_{eff} = \frac{\mu^f_{eff}\mu_s}{\mu^f_{eff}(1-\phi) + \mu_s\phi}, \tag{43}$$

$$\mu^{agg}_{BG} = \frac{\mu_{BG}\mu_s}{\mu_{BG}(1-\phi) + \mu_s\phi}, \tag{44}$$

where μ_{BG} is derived using Eq. (40) and substituting $\dot{\varepsilon}_{BG}$ instead of using $\dot{\varepsilon}^f_{xx}$. The ratio between effective aggregate viscosity μ^{agg}_{eff} and background aggregate viscosity μ^{agg}_{BG} indicates how much smaller the effective aggregate viscosity inside a two-phase 1D system is. This, in turns, results in a higher strain rate of the aggregate $\dot{\varepsilon}^{agg}_{eff}$ (according to Eq. (36)). The ratio is dependent on fluid fraction ϕ and the power law coefficient n in the following way

$$\frac{\mu^{agg}_{eff}}{\mu^{agg}_{BG}} = (\phi)^{(1/n-1)}. \tag{45}$$

Thus, the dependence on the fluid fraction ϕ and its exponent $(1/n-1)$ results from the higher strain rates occurring inside the aggregate compared to the applied background strain rate. The relation of the additional exponent of 1.8 for spheres or 2.8 for hexagons remains to be explained. However it seems that it is strongly related to the shape of the particles as described in Section 3.1.1. Similarly, the ratio $\dot{\varepsilon}^{agg}_{eff}/\dot{\varepsilon}_{BG}$ will be higher than 1. With this fact, we can additionally explain the dependence of the maximum occurring strain rate on fluid fraction and the background strain rate inside a two-phase system as shown in Section 5.1.

References

Arbaret, L., Bystricky, M., Champallier, R., 2007. Microstructures and rheology of hydrous synthetic magmatic suspensions deformed in torsion at high pressure. J. Geophys. Res.-Solid Earth 112 (B10).

Arzi, A.A., 1978. Critical phenomena in the rheology of partially melted rocks. Tectonophysics 44, 173–184.

Bagdassarov, N.S., Dorfman, A.M., Dingwell, D.B., 1996. Modelling of melt segregation processes by high-temperature centrifuging of partially molten granites—II. Rayleigh–Taylor instability and sedimentation. Geophys. J. Int. 127, 627–634.

Biot, M., Odé, H., 1965. Theory of gravity instability with variable overburden and compaction. Geophysics 30, 153–166.

Brady, J.F., Bossis, G., 1988. Stokesian dynamics. Annu. Rev. Fluid Mech. 20, 111–157.

Burg, J.P., Kaus, B., Podladchikov, Y., 2004. Dome structures in collision orogens. Mechanical investigation of the gravity/compression interplay. In: Whitney, D., Teyssier, C., Siddoway, C. (Eds.), Gneiss Domes in Orogeny, vol. 380. Geological Society of America, Boulder, pp. 47–66.

Caricchi, L., Burlini, L., Ulmer, P., Gerya, T.V., Vassalli, M., Papale, P., 2007. Non-Newtonian rheology of crystal-bearing magmas and implications for magma ascent dynamics. Earth Planet. Sci. Lett. 264, 402–419.

Champellier, R., Bystricky, M., Arbaret, L., 2008. Experimental investigation of magma rheology at 300 MPa: from pure hydrous melt to 76 vol. crystals. Earth Planet. Sci. Lett. 267 (3–4), 571–583.

Cleary, P.W., 2008. The effect of particle shape on simple shear flows. Powder Technol. 179, 144–163.

Cordonnier, B., Hess, K.-U., Lavallee, Y., Dingwell, D., 2009. Rheological properties of dome lavas: case study of Unzen volcano. Earth Planet. Sci. Lett. 279 (3–4), 263–272.

Costa, A., 2005. Viscosity of high crystal content melts: dependence on solid fraction. Geophys. Res. Lett. 32 (L22308). doi:10.1029/2005GL024303.

Costa, A., Caricchi, L., Bagdassarov, N., 2009. A model for the rheology of particle-bearing suspensions and partially molten rocks. Geochem. Geophys. Geosyst. 10 (3). doi:10.1029/2008GC002138.

Cuvelier, C., Segal, A., van Steemhoven, A., 1986. Finite Element Methods and Navier–Stokes Equations. Mathematics and Its Applications. D. Reidel Publishing company, Dordrecht.

Dabrowski, M., 2008. Anisotropy and heterogeneity in finite deformation — resolving vs. upscaling. Ph.D. thesis, University of Oslo, Physics of Geological Processes, Sem Selands vei 24, NO-0316 Oslo, Norway.

Dabrowski, M., Krotkiewski, M., Schmid, D.W., 2008. MILAMIN: MATLAB-based FEM solver for large problems. Geochem. Geophys. Geosyst. 9. doi:10.1029/2007GC001719.

Dabrowski, M., Schmid, D.W., Podladchikov, Y.Y., 2009. Mechanical Anisotropy Development of a Two-Phase Composite Subject. Geophys. Res. Abstr. 11 (EGU2009-5768) http://meetingorganizer.copernicus.org/EGU2009/EGU2009-5768.pdf.

Deubelbeiss, Y., Kaus, B.J.P., 2008. Comparison of Eulerian and Lagrangian numerical techniques for the Stokes equations in the presence of strongly varying viscosity. Phys. Earth Planet. Inter. 171 (1–4), 92–111.

Einstein, A., 1906. Eine neue Bestimmung der Molekuldimensionen. Ann. Phys. 19, 289–306.

Gay, E.C., Nelson, P.A., P., A.W., 1969. Flow properties of suspensions with high solids concentration. AIChE J. 15 (6), 815–822.

Golabek, G.J., Gerya, T.V., Kaus, B.J.P., Ziethe, R., Tackley, P.J., in press. Rheological controls on the terrestrial core formation mechanism. Geochem. Geophys. Geosyst., 10, Q11007. doi:10.1029/2009GC002552.

Hess, K.U., Cordonnier, B., Lavalée, Y., Dingwell, D.B., 2008. Viscous heating in rhyolite: A in situ experimental determination. Earth Planet. Sci. Lett. 275, 121–126.

Jeffrey, D.J., Acrivos, A., 1976. The rheological properties of supsensions of rigid particles. AIChE J. 22 (3), 417–432.

Kaus, B.J.P., 2005. Modelling approaches to geodynamic processes. Ph.D. thesis, ETH Zürich, doi:10.3929/ethz-a-004946413, diss. ETH No. 15860.

Krieger, I.M., 1972. Rheology of monodisperse lattices. Adv. Colloid Interface Sci. 3 (2), 111–136.

Krieger, I.M., Dougherty, T.J., 1959. A mechanism for non-Newtonian flow in suspensions of rigid spheres. Trans. Soc. Rheol. (III), 137–152.

Lejeune, A.-M., Richet, P., 1995. Rheology of crystal bearing silicate melts: an experimental study at high viscosities. J. Geophys. Res. 100 (B3), 4215–4229.

Marsh, B.D., 1981. On the crystallinity, probability of occurrence, and rheology of lava and magma. Contrib. Mineral. Petrol. 78, 85–98.

McKenzie, D.P., 1984. The generation and compaction of partially molten rock. J. Petrol. 25 (3), 713–765.

Petford, N., 2009. Which effective viscosity? Mineral. Mag. 73, 167–191.

Phan-Thien, N., Tran-Cong, T., Graham, A.L., 1991. Shear flow of periodic arrays of particle clusters: a boundary–element method. J. Fluid Mech. 288, 275–293.
Pinkerton, H., Stevenson, R.J., 1992. Methods determining the rheological properties of magmas at sub-liquidus temperatures. J. Volcanol. Geotherm. Res. 53, 47–66.
Popov, A., Sobolev, S., 2008. SLIM2D: a tool for three-dimensional thermomechanical modeling of lithospheric deformation with elasto-visco-plastic rheology. Phys. Earth Planet. Inter. 171 (1–4), 55–57.
Ramberg, H., 1968. Fluid dynamics of layered systems in the field of gravity, a theoretical basis for certain global structures and isostatic adjustment. Phys. Earth Planet. Inter. 1, 63–87.
Ranalli, G., 1995. Rheology of the Earth, 2nd Edition. Chapman and Hall, London.
Ranalli, G., 1997. Rheology of the lithosphere in space and time. Geol. Soc., Lond. Spec. Publ. 121, 19–37.
Roscoe, R., 1952. The viscosity of suspensions of rigid spheres. Br. J. Appl. Phys. 3, 267–269.
Rutgers, I.R., 1962a. Relative viscosity of suspensions of rigid spheres in newtonian liquids. Rheol. Acta 3, 202–210.
Rutgers, I.R., 1962b. Relative viscosity and concentration. Rheol. Acta 4, 305–348.
Saar, M.O., Manga, M., Cashman, K.V., Fremouw, S., 2001. Numerical models of the onset of yield strength in crystal-melt suspension. Earth Planet. Sci. Lett. 187, 367–379.
Schmid, D.W., Podladchikov, Y., 2003. Analytical solutions for deformable elliptical inclusions in general shear. Geophys. J. Int. 155, 269–288.
Shewchuk, J., 1996. Applied Computational Geometry: Towards Geometric Engineering. Vol. 1148 of Lecture Notes in Computer Science. Springer-Verlag, http://www.cs.cmu.edu/ quake/triangle.html, Ch. Triangle: Engineering a 2D Quality Mesh Generator and Delaunay Triangulator, pp. 203–222, From the First ACM Workshop on Applied Computational Geometry.
Slezkin, A., 1955. Dynamics of Viscous Incompressible Fluid. Gostekhizdat, Moscow.
Stickel, J.J., Powell, R.L., 2005. Fluid mechanics and rheology of dense suspensions. Annu. Rev. Fluid Mech. 37, 129–149.
Vand, V., 1948. Viscosity of solutions and suspensions. II. Experimental determination of the viscosity concentration function of spherical suspensions. J. Phys. Chem. 52 (2), 300–314.
Völtz, C., Nitschke, M., Heymann, L., Rehberg, I., 2002. Thixotropy in macroscopic suspensions of spheres. Phys. Rev. 65. doi:10.1103/PhysRevE.65.051402.
Ward, S.G., Whitmore, R.L., 1950. Studies of the viscosity and sedimentation of suspensions. Br. J. Appl. Phys. 1, 325–328.
Webb, S.L., Dingwell, D.B., 1990. Non-Newtonian rheology of igneous melts at high stresses and strain rates: experimental results for rhyolite, andesite, basalt and nephielinite. J. Geophys. Res. 95 (B10), 695–701.
Whitehead, J.A., 1988. Fluid models of geological hotspots. Annu. Rev. 20, 61–87.